JOURNAL OF GEOPHYSICAL RESEARCH, VOL. 101, NO. C10, PAGES 22,495–22,512, OCTOBER 15, 1996

Local ocean response to a multiphase westerly wind burst
1. Dynamic response

W. D. Smyth
College of Oceanic and Atmospheric Sciences, Oregon State University, Corvallis

D. Hebert
Graduate School of Oceanography, University of Rhode Island, Narragansett

J. N. Moum
College of Oceanic and Atmospheric Sciences, Oregon State University, Corvallis

Abstract. The dynamic response to a westerly wind burst which occurred during the Coupled Ocean Atmosphere Response Experiment in the warm pool of the equatorial Pacific Ocean is described using velocity, hydrography, and microstructure measurements. Turbulent fluxes distributed momentum input from the wind over a near-surface layer of variable thickness. Coriolis and pressure gradient terms combined to induce a wavelike response whose frequency was close to the local inertial frequency. Wind stress variations on near-inertial timescales interfered both constructively and destructively with the wave response, exerting considerable influence on the observed currents.

1. Introduction

Westerly wind bursts (WWBs) in the western equatorial Pacific Ocean are potentially important in triggering and sustaining El Niño–Southern Oscillation events. WWBs also provide the most energetic mechanism for maintaining the mixed layer in the western Pacific warm pool [*Lukas and Lindstrom,* 1991]. In addition to accelerating surface currents toward the east, WWBs tend to generate westward currents near the thermocline which, combined with the surface current, create strong vertical shear at depth [*McPhaden et al.,* 1988, 1992; *Delcroix et al.,* 1993; *Zhang,* 1995] and thereby generate intense mixing well below the surface. To date, observations of WWBs have not included microstructure measurements, so the role of turbulent mixing in modulating the ocean's response to the surface forcing had to be inferred indirectly [e.g., *McPhaden et al.,* 1988]. In this paper and in a companion paper [*Smyth et al.,* this issue] (hereinafter referred to as SHM2), we describe the ocean's response to the first such event for which detailed observations, including microstructure data, are available [*Moum and Caldwell,* 1994].

Our observations were made as part of the ocean component of the Tropical Ocean-Global Atmosphere-Coupled Ocean Atmosphere Response Experiment (TOGA-COARE). One of the primary goals of COARE was [Webster and Lukas, 1992, pp. 1394–1395] "to describe and understand the ocean's response to combined buoyancy and wind stress forcing in the western Pacific warm pool region." Understanding the response to WWBs is clearly an important aspect of this objective, and it is fortunate that such an event occurred during the intensive observation period of COARE.

In SHM2, we discuss the impact of the WWBs on the thermohaline structure of the upper ocean. This paper will cover some dynamical aspects of the ocean's response to the WWBs, primarily via the evaluation of terms in the equations governing zonal and meridional momentum. A discussion of observations and processing methods (section 2) is followed by an overview of the observations (section 3). In section 4, we describe a near-inertial oscillation which appears to be a response to the wind forcing. Turbulent momentum fluxes are discussed in section 5, as a prelude to our interpretation of the local dynamics in terms of zonal and meridional momentum budgets (section 6). A summary of these observations is given in section 7.

2. Experimental Details

The observations discussed here were made from R/V *Moana Wave*, which held station at 1°45′S, 156°E from December 20, 1992, to January 12, 1993. This was the approximate location of a surface mooring (which included sensors to measure surface meteorological pa-

Paper number 96JC02005.
0148-0227/96/96JC-02005$09.00

rameters and subsurface currents, temperature, and conductivity) deployed to provide longer-term measurements throughout the COARE intensive observation period [*Weller and Anderson,* 1996]. During the time we remained on station, we stayed within 10 km of this mooring at all times to ensure that we had nearly coincident measurements for comparison.

Microstructure measurements were made from the CHAMELEON profiler [*Moum et al.,* 1995], deployed from the stern of *Moana Wave.* Profiles to 250 m depth were made every 6–10 min. Temperature T, salinity S, potential density σ_θ, Brunt-Väisälä frequency N, turbulent kinetic energy (TKE) dissipation rate ϵ, and temperature variance dissipation rate χ were computed using these data. Horizontal currents were measured using a 150-kHz RD Instruments shipboard acoustic Doppler current profiler (ADCP), with 8-m pulse length and 4-m bin width. Hourly averaged currents are accurate to within $\sim$1 cm s^{-1}, the primary source of uncertainty being the high vertical shear [e.g., *Lien et al.,* 1994]. The squared vertical shear Sh^2 and gradient Richardson number ($Ri = N^2/Sh^2$) were computed from hourly averaged profiles of velocity and density. Vertical derivatives were approximated by centered differences between 4-m depth bins. Measurements of surface meteorology (including eddy-correlation flux measurements) were made from *Moana Wave* by C. Fairall and G. Young and kindly provided for our use. From these measurements, heat and buoyancy fluxes and the surface stress were estimated on hourly averages using the COARE version 2 algorithm [*Fairall et al.,* 1996].

Our preferred method of operation was to steam slowly into the wind, making as little way over land as possible while maintaining ship steering capability. This provided unobstructed measurements of surface meteorology for all of the mast-mounted sensors on the bow. To stay within 10 km of the surface mooring, however, we periodically had to make downwind runs. While this means of deployment has been straightforward in many other locations, the strong and intermittent squalls that dominated the surface forcing during the wind burst created considerable ship-handling difficulties. The wind signature of line squalls resulted in a dramatic increase in ship-based observed wind from background (5 m s^{-1}, for example) to more than 20 m s^{-1} in a period of several minutes. Once the peak wind had passed, there followed turbulent gusts from all directions. This caused us two serious problems. While deploying CHAMELEON from the stern, the squall front wind sometimes forced the ship backward; in one squall in which instantaneous wind speeds of 34 m s^{-1} were observed, the ship actually was forced backward over CHAMELEON, leaving it stuck beneath the ship. Thanks to quick thinking and perseverance by some members of our group, we were able to recover it with only minor damage. We had also deployed a surface layer, instrumented platform alongside the ship. However, in a squall with especially energetic turbulent gusts in which the wind increased by 20 m s^{-1} and changed direction by 90° in a period of about 15 s, the ship was driven sideways into the platform, destroying it and resulting in a dramatic nighttime recovery on Christmas Eve.

3. Overview

In this section, we present an overview of the data gathered during the cruise, reserving detailed analysis and interpretation for later sections. In cruise-averaged profiles, potential temperature θ, salinity S, and potential density σ_θ were nearly constant over the upper 60 m (Figure 1a). Below this level, a layer of strong vertical gradients (in all three quantities) extended to $\sim$120 m. The apparent thickness of this pycnocline is increased by the averaging process, since the layer was displaced vertically through several tens of meters by internal wave motions, primarily the semidiurnal tide. Instantaneously, pycnocline thickness (defined by $N^2 > 10^{-4}$ s^{-2}; see Figure 5a) was typically of the order of 20–40 m. Below the pycnocline, salinity remained roughly constant with depth (in the mean), while temperature continued to decrease. In the cruise-averaged profiles, we see no indication of the "barrier layer" (i.e., a thin layer of stable haline stratification in a region of negligible thermal stratification, thus a "barrier" to the vertical mixing of heat) found by *Lukas and Lindstrom* [1991]. However, density stratification due to salinity differences is generally of similar magnitude to that due to temperature differences, so we expect salt stratification to play an important role in governing the response to surface forcing (SHM2).

The cruise-averaged zonal current had a complex structure in the upper 200 m (Figure 1b). The average current was directed slightly to the left of the local wind, which was dominated during the cruise by a westerly wind burst. Near the depth of the thermocline was a westward current which may have been the southern extension of the South Equatorial Current appearing beneath the shallower wind-driven currents or may have been part of the dynamic response to the wind burst [*McPhaden at al.,* 1988]. Below this was the southern edge of the Equatorial Undercurrent (EUC). Meridional velocities were small in the mean, although important dynamically on shorter timescales, as will be argued in section 6. The time integral of the 14-m current during the cruise was 700 km to the east, 200 km to the north. The integrated zonal current observed here is about one fifth of the warm-pool displacement observed during the 1986–1987 El Niño event [*McPhaden and Picaut,* 1990].

The cruise-averaged N^2 profile was dominated, as expected, by strong stratification in the pycnocline (Figure 1c). Mean stratification was relatively weak near the surface ($N^2 < 5 \times 10^{-5}$s^{-2} for depth $z > -50$ m) but increased sharply in the upper 15 m. Enhanced stratification near the surface appears to have been associated with the following two mechanisms: (1) haline stratification resulting from intense rainfall and (2) thermal stratification due to the combination of weak winds and surface warming which dominated during the later stages of the cruise (compare with SHM2; Figure

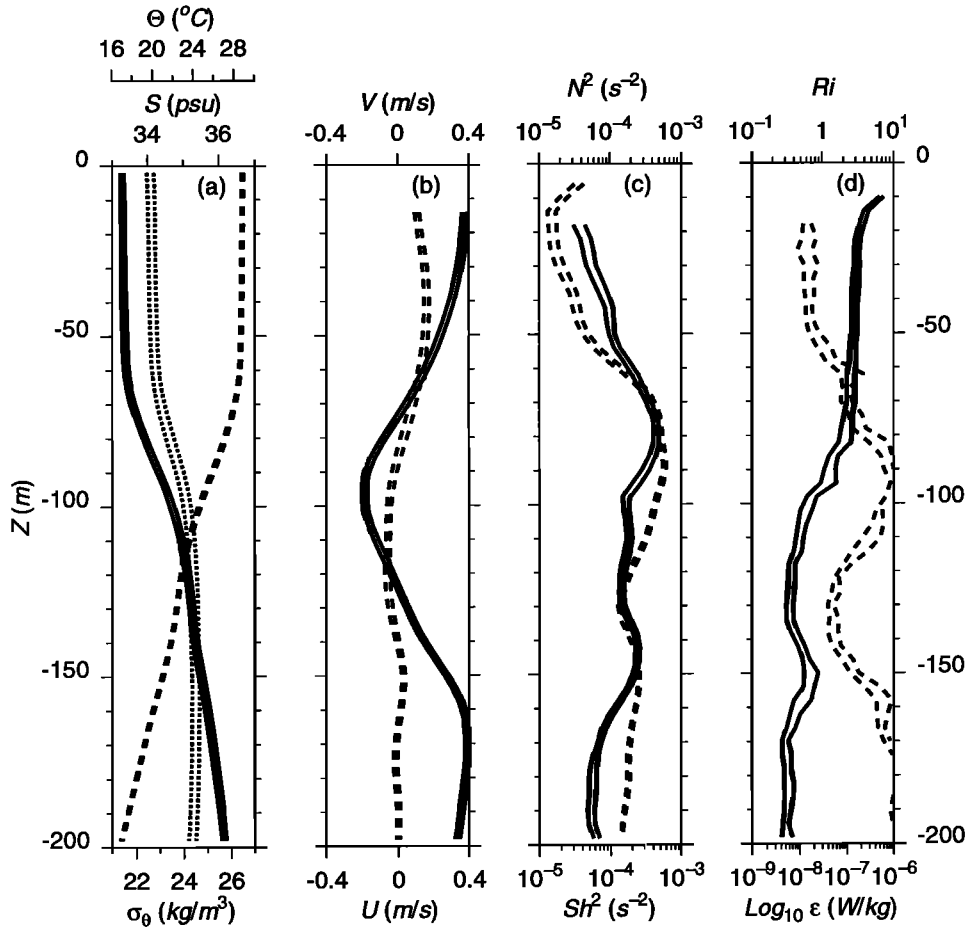

Figure 1. Cruise-averaged profiles of (a) potential temperature T (dashed curves), salinity S (dotted curves), potential density σ_θ (solid curves), (b) zonal velocity V (solid curves), meridional velocity U (dashed curves), (c) squared shear Sh^2 (solid curves), Brunt-Väisäla frequency N^2 (dashed curves), (d) Richardson number Ri (dashed curves), and dissipation rate ϵ (solid curves). Each pair of curves represents the 95% bootstrap confidence limits [*Efron and Tibshirani*, 1993] on the mean profile. (Sh^2 and Ri were computed using hourly averaged data, then averaged over the cruise.)

2). The mean square vertical shear Sh^2 was largest in the upper thermocline, but stratification in that region was sufficient to make the mean gradient Richardson number ($Ri = N^2/Sh^2$) large (Figure 1d). Associated with the increase in mean Richardson number was an order-of-magnitude decrease in TKE dissipation rate ϵ across the thermocline. Above the thermocline, dissipation rates were of the order of 10^{-7} W kg^{-1}, increasing gradually toward the surface. Above ~15 m, ϵ increased more sharply.

Wind stress was dominated by a period of intense winds, which lasted roughly from December 20 to January 4 (Figure 2a). Wind records from the nearby Improved Meteorological Instrument (IMET) buoy [*Weller and Andersen*, 1996, Figure 6] show that winds were weak for several days prior to our arrival on December 20, although a moderate wind episode occurred during December 13-16. Strong winds appeared in three distinct intervals, each lasting between 3 and 5 days. We will refer to the wind event which extended from December 20 to January 4 (inclusive) as "the" wind burst and to the shorter windy periods within that interval as "phases 1, 2, and 3" of the wind burst. The three intervals shown by solid bands at the top of Figure 2a will be used in later calculations to represent phases 1, 2, and 3. The gray-shaded bands indicate intervening periods of relative calm. The period of milder weather following January 4 will be called the "recovery phase." As is shown by the arrows on Figure 2a, the winds were predominantly from the west, though a significant northerly component appeared toward the end of phase 3.

Significant rainfall (Figure 2b) occurred during the following four intervals: (1) throughout the first phase of the wind burst, (2) near the beginning of phase 2, (3) between phases 2 and 3, and (4) at the beginning of the recovery phase. Most precipitation was concentrated in intense squalls of 15–30 min duration (as described in section 2). During the first half of the wind burst, the surface heat flux was predominantly upward (out of the

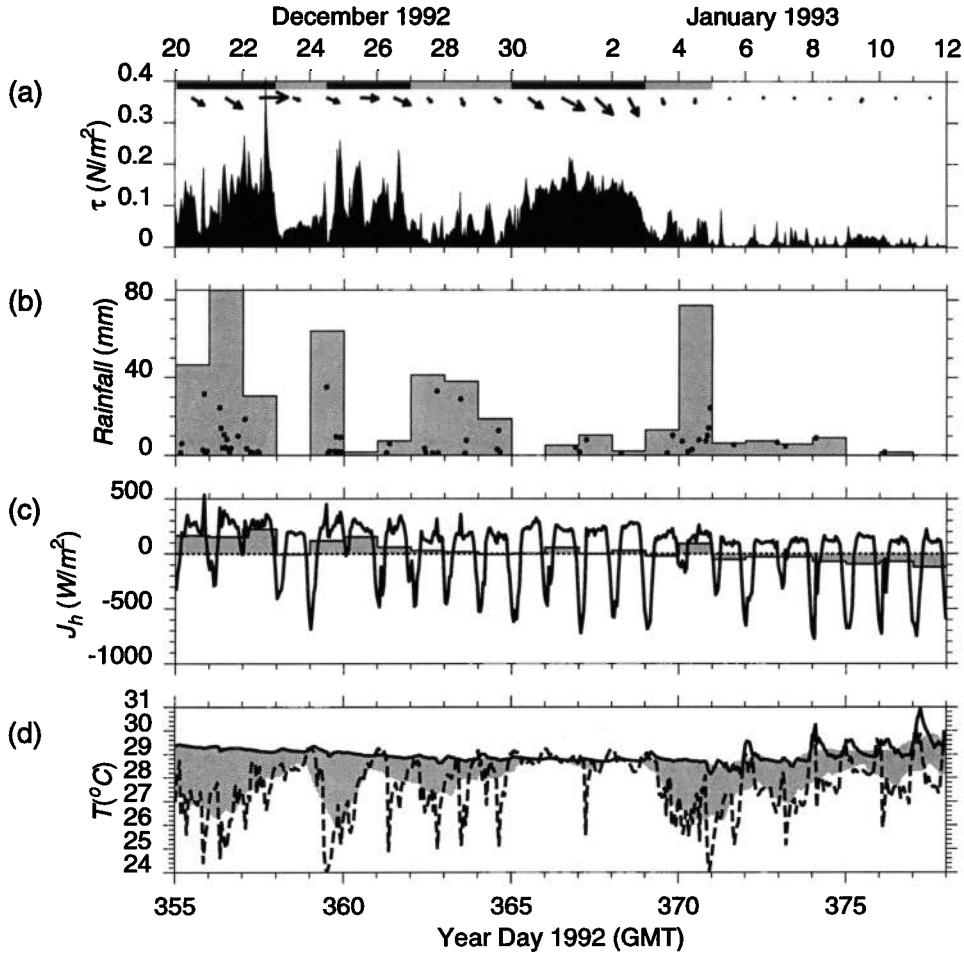

Figure 2. (a) Squared magnitude of the wind stress. Arrows indicate daily averaged stress; arrow to the right denotes eastward. The intervals indicated by the solid and gray-shaded bands at the top are used in the text to approximate phases 1, 2, and 3 of the wind burst and the adjacent periods of relative calm. (b) Rainfall (hourly denoted by circles, daily denoted by shading). (c) Total surface heat flux (hourly average denoted by gray, daily average denoted by solid curve). (d) Sea surface temperature (solid curve) and air temperature (dashed curve). The boundaries of the shaded region indicate 24-hour running means.

ocean), with daily averaged values reaching 200 W m^{-2} (Figure 2c). During the second half of the wind burst, the daily averaged flux was close to zero. The surface flux was predominantly downward in the recovery period. The atmosphere was generally cooler than the sea surface; the average temperature differential was 1.25°C (Figure 2d). Sea surface temperature (SST) decreased during the wind burst (the net cooling was ~1°C), then increased rapidly during the recovery phase, exhibiting a strong diurnal variation. Subsurface processes which influence the response of SST to surface forcing are discussed in detail in SHM2.

Cooling associated with the wind burst was evident down to ~60 m (Figure 3a). In the latter stages of the wind burst, the top of the thermocline descended from 60 to ~90 m. Following the cessation of strong winds, the thermocline shallowed rapidly and restratification was apparent in the surface layer. Similar behavior was evident in the salinity and density fields (Figures 3b and 3c). The near-surface haline structure featured fresh pools which were often (though not always) coincident with local rainfall. Below the main halocline, salinity generally increased to a maximum between 100 and 150 m (in the vicinity of the EUC). Short-period oscillations in T, S, and σ were due primarily to the semidiurnal tide.

Horizontal currents (Figure 4) were dominated by a strong semidiurnal oscillation plus fluctuations on longer timescales. Zonal accelerations in the surface layer generally followed the wind stress; the surface current increased from near zero to speeds in excess of 0.7 m s^{-1} eastward near the end of the wind burst. Below the surface layer (i.e., at 100 m), westward flow oscillated in speed with a period of 10-12 days. Below that was a layer of eastward flow associated with the EUC. The meridional current exhibited little or no direct relationship with the wind stress. Near the surface, we observed two periods of northward velocity, each of which

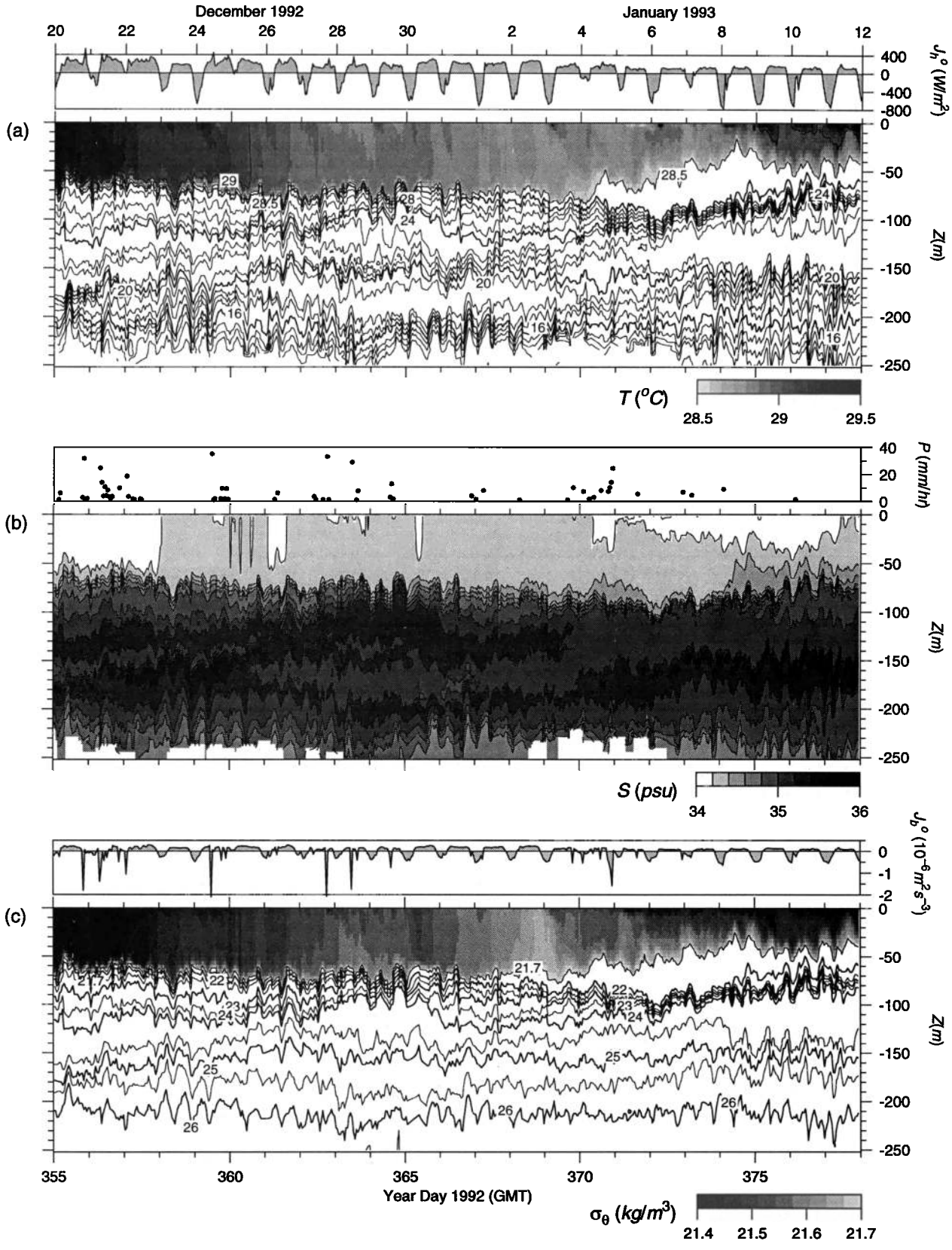

Figure 3. (a) Temperature. Values above 28.5°C are shaded at 0.05°C intervals. The contour interval is 1°C, with an added contour at 28.5°C. (b) Salinity. Contour interval is 0.2 practical salinity units (psu). (c) Potential density. Values below 21.7 kg m^{-3} are shaded at 0.025 kg m^{-3} intervals. Otherwise, the contour interval is 0.5 kg m^{-3}. Profiler data were averaged into 1-hour, 4-m bins before contouring. For reference, the hourly surface heat flux, precipitation, and buoyancy flux are included in Figures 3a, 3b, and 3c (top), respectively.

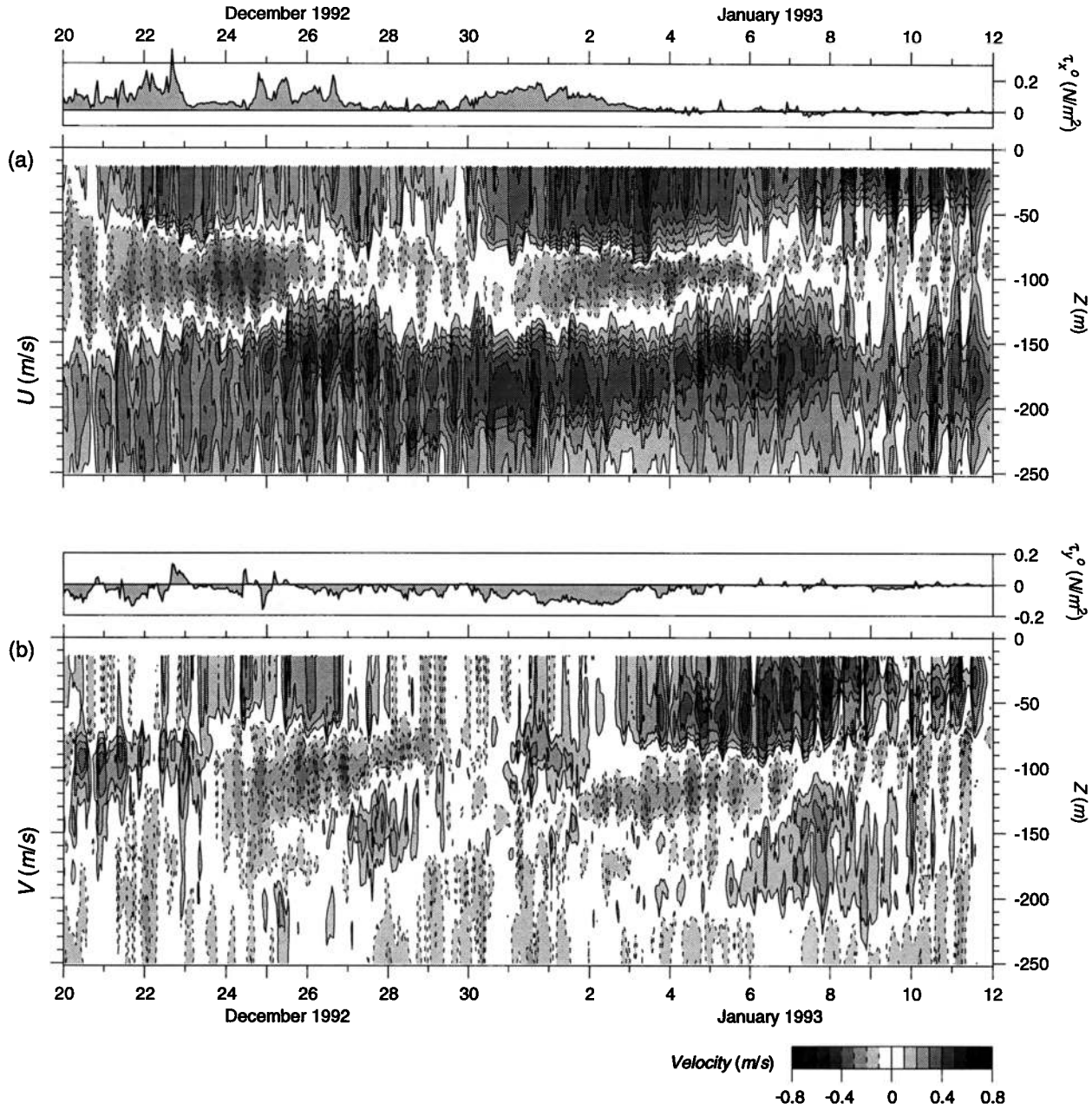

Figure 4. (a) Zonal current. (b) Meridional current. Contours represent $\pm 10, \pm 20, \ldots$ cm s^{-1}. Dashed contours indicate negative values. Current data are from shipboard acoustic Doppler current profilers and are averaged into 1-hour, 4-m bins. For reference, hourly averaged zonal and meridional wind stresses are shown in Figures 4a and 4b (top), respectively.

appeared following a period of strong eastward flow. Analysis of the momentum budget (see section 6) will show that this acceleration was the northward veering of the wind-driven eastward currents due to the Coriolis force. Below ~50 m, the meridional flow exhibited an oscillatory pattern, with upward phase propagation, an amplitude of ~0.2 m s^{-1}, and a period somewhat in excess of 10 days (as is also evident in the zonal current). This wavelike feature is discussed in detail in the next section.

A region of intense stratification was evident in the thermocline during the recovery phase, with N^2 reaching values well in excess of 10^{-3}s^{-2} (N = 18 cph) (Figure 5). Squared shear of similar magnitude was seen at the base of the surface layer during the final days of the wind burst (January 1–6, 70–100 m). The ~10-day oscillation prominent in Figure 4 was also evident in the shear and in N^2. The diurnal mixing cycle [e.g., *Moum et al.*, 1989; *Schudlich and Price*, 1992] was evident in the upper 70 m during periods of strong wind. The white-colored regions near the surface indicate $N^2 < 10^{-6}$s^{-2} (N = 0.57 cph). In the nocturnal mixed layer, Ri frequently decreased below 1/4 for periods of several hours. We also observed regions of low

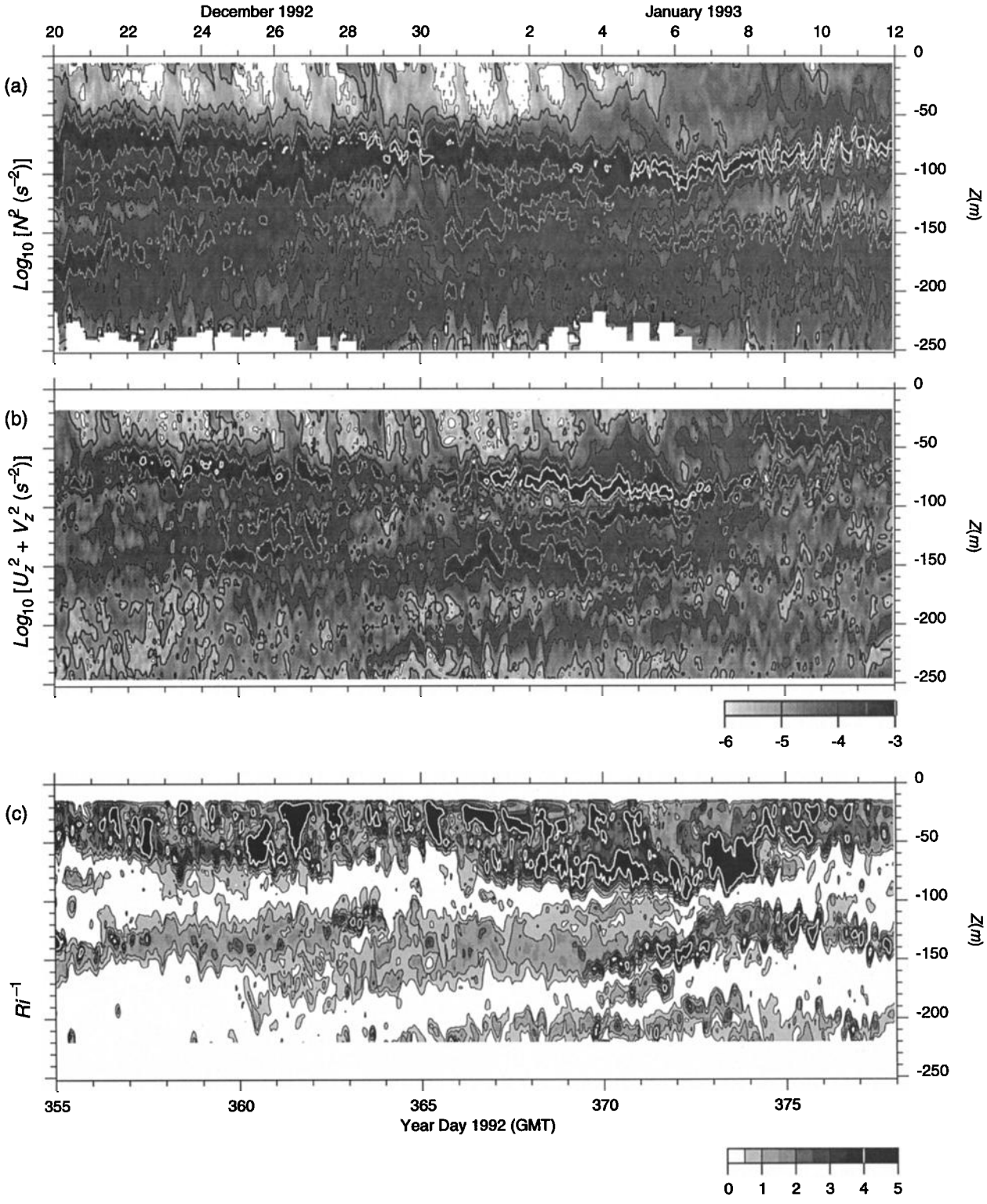

Figure 5. Time-depth sections of (a) squared Brunt-Väisäla frequency, (b) squared magnitude of the vertical shear, and (c) gradient Richardson number $Ri = N^2/(U_z^2 + V_z^2)$. The scale below Figure 5b applies to both Figures 5a and 5b. Vertical derivatives were approximated by 8-m finite differences averaged over 4 m (i.e., centered differences between 4-m bins). Black contours indicate the values 10^{-6}, 10^{-5}, and 10^{-4} s^{-2}. White contours indicate the values $10^{-3.5}$ and 10^{-3} s^{-2}. The white contours in Figure 5c enclose regions in which $Ri < 1/4$.

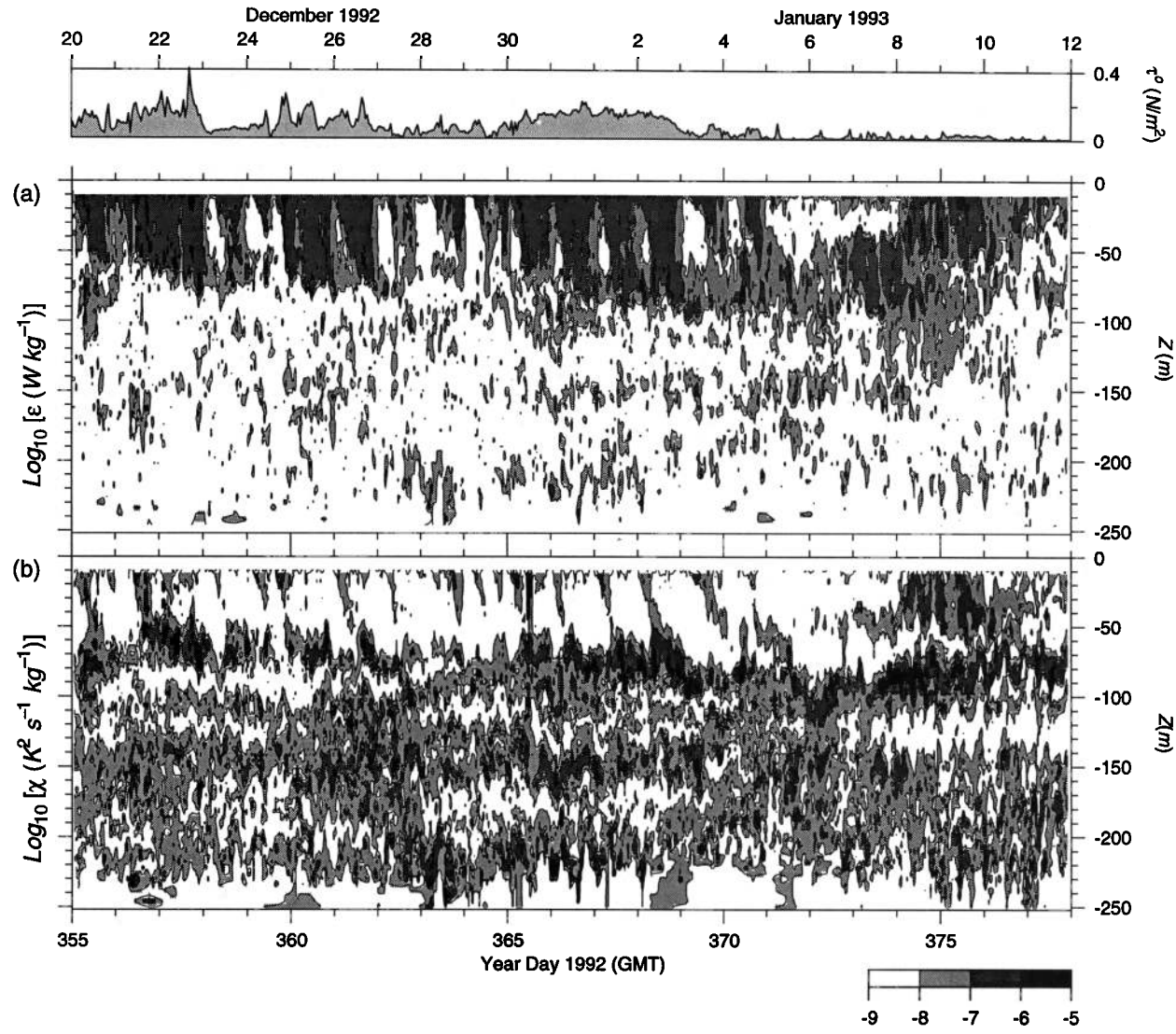

Figure 6. (a) Turbulent kinetic energy dissipation rate ϵ. (b) Temperature variance dissipation rate χ. For reference, the wind stress magnitude is given (top).

Ri near the base of the surface layer during and after the wind burst; this was a consequence of the high shear at the base of the wind-driven current. Deeper regions of low *Ri* were associated with the shear zones on the upper and lower flanks of the EUC.

Near the surface, both ϵ and χ showed a strong diurnal variation whose amplitude and depth penetration was clearly modulated by the wind stress (Figure 6). During periods of strong wind, regions of particularly strong turbulence occurred each evening at the base of the mixed layer as it descended. Turbulence was often, though not always, associated with low Richardson number (see Figure 5c). The relationship is evident, for example, in the turbulent layer near 70 m, where ϵ increased to a maximum on January 7, several days after the diurnal mixing cycle associated with the wind burst had subsided.

4. Near-Inertial Oscillations

Eriksen [1993] has computed the linear response to an idealized, translating, westerly wind burst, and the results of that calculation provide a useful context within which to interpret our observations. Eriksen found that the dynamic response to a wind burst centered on the equator has two parts: (1) a Yoshida jet and (2) a wake consisting of gravity and mixed Rossby-gravity waves. The jet tends to dominate the response near the equator, while the wave wake dominates farther to the north and south. (This relationship is somewhat more complicated when the wind burst is asymmetric about the equator.) The dominant frequency of the wave wake is relatively insensitive to wind burst geometry and time dependence and appears instead as a slowly varying function of latitude closely related to the local Cori-

olis frequency. At the latitude of our station (1°45'S), the inertial period is 16.3 days and the dominant period of the wave wake is predicted to be 12 days [*Eriksen*, 1993, Figure 7].

Horizontal currents (Figure 4) exhibited a clear semidiurnal signal, as well as oscillations at other frequencies. The zonal currents divided naturally into three depth intervals.

1. From the surface to a depth of ~40–70 m, the zonal current remained close to its near-surface value, which was clearly associated with the zonal surface stress. A temporary acceleration appeared in the wake of each phase of the wind burst. However, the magnitude of the current response following each interval of strong winds exhibited no obvious relation to the strength of the wind. Phase 1 drove a zonal current of magnitude 0.3–0.4 m s^{-1}, while phase 2 led to a much smaller acceleration. Phase 3 generated a pronounced acceleration to speeds in excess of 0.6 m s^{-1}. The reason for these discrepancies will become clear when we examine the momentum budgets. Meridional currents exhibited northward accelerations (in the direction of the Coriolis force) following the eastward acceleration associated with each phase of the wind burst. The meridional current, like the zonal current, remained similar to its surface value in this layer. Unlike the zonal current, the meridional flow exhibited no direct relationship with the wind stress.

2. A second layer extended from ~70 to ~120 m. It was distinguished by predominantly westward current whose amplitude was maximum during two periods, roughly 10 days apart.

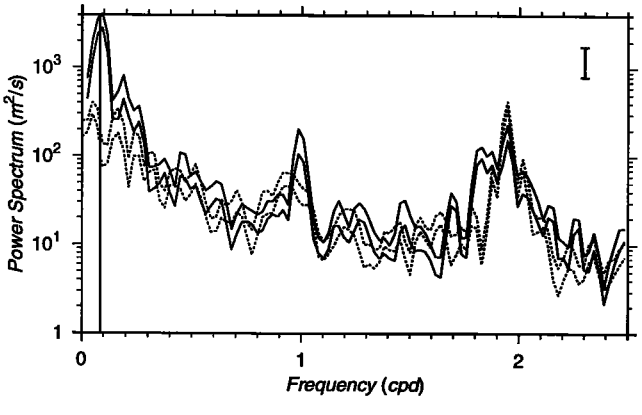

Figure 7. Average rotary power spectra for horizontal currents between 14 and 210 m. Spectra were computed (with cosine-bell windowing) for individual 4-m depth bins, then averaged. Pairs of curves indicate 95% bootstrap confidence limits [*Efron and Tibshirani*, 1993] on the depth average. The error bar at top right indicates the spread in the 95% uncertainty limits (4 times the standard deviation) for a single estimate of the power spectrum, assuming 25 degrees of freedom. Solid curves denote anticyclonic (counterclockwise) rotation. Dotted curves denote cyclonic rotation. The vertical line indicates the 12-day period predicted by *Eriksen*'s [1993] linear model.

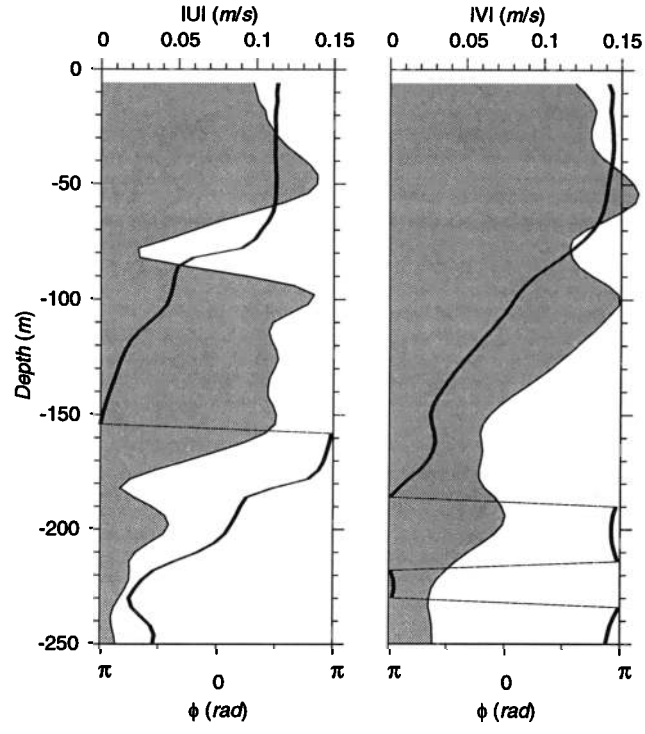

Figure 8. Depth dependence of the Fourier mode having frequency $f = 0.0833$ cpd for zonal and meridional currents. Shaded curve is amplitude; solid curve is phase.

3. The third layer was dominated by the EUC. In both the second and third layers, the meridional flow was dominated by an oscillatory pattern with period of order 10 days and ascending phase propagation, upon which was superimposed the ubiquitous semidiurnal tide.

Rotary power spectra for the horizontal currents were computed for each 4-m depth bin, and the resulting spectra were averaged together (Figure 7). The dominant peak in the velocity spectra is consistent with the near-inertial period predicted by linear theory (although the length of the time series is insufficient to allow us to distinguish with certainty between the predicted 12-day period and 16.3 days, the local inertial period). The sense of the near-inertial oscillation was anticyclonic, which *Eriksen*'s [1993] model also predicts. There is a striking contrast between the zonal and meridional currents at the 12-day period (Figure 8). The zonal current changed sign abruptly at $z = -80$ m and again at $z = -180$ m. In contrast, the meridional oscillation exhibited a smooth upward phase propagation below the top of the pycnocline. These contrasting behaviors are also apparent in the time-depth sections shown in Figure 4 and were probably a consequence of the strong vertical shear in the mean zonal flow (see Figure 1). Upward phase propagation is consistent with downward energy propagation and hence suggests that the wave was driven by surface forcing. Thus the frequency, the sense of the oscillation, and the direction

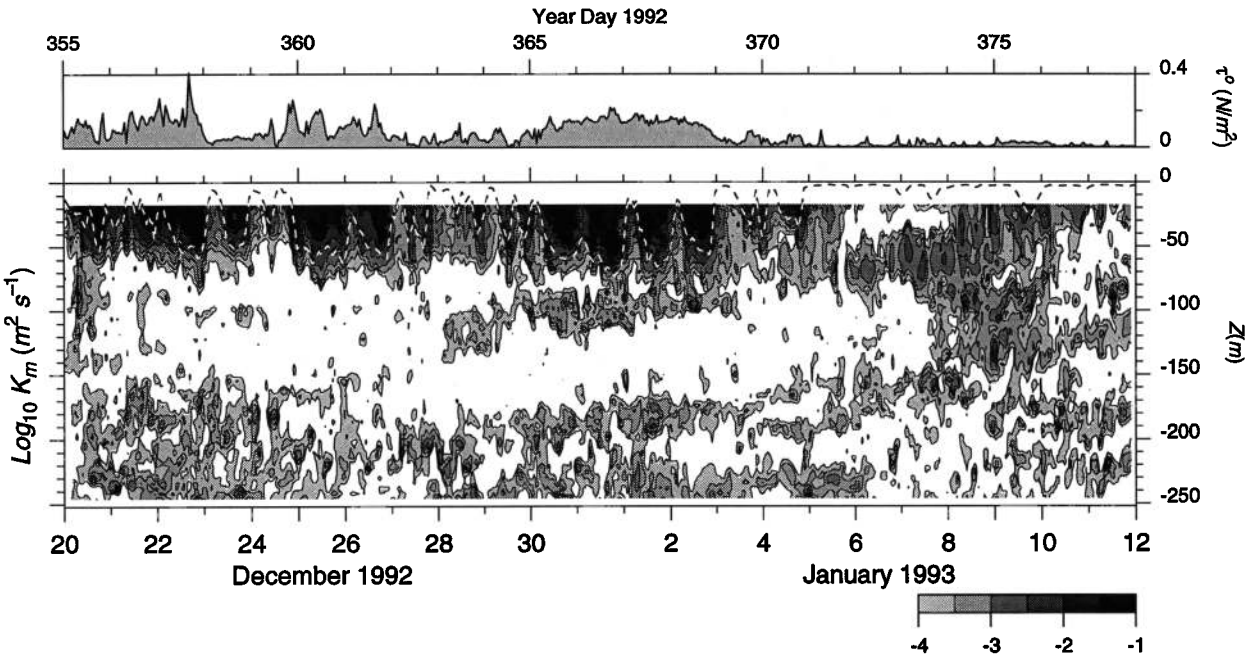

Figure 9. Time-depth section of the turbulent viscosity K_m. The dashed line indicates the depth of the diurnal mixed layer [*Smyth et al.*, this issue]. For reference, the wind stress magnitude is given (top).

of phase propagation all suggest that the near-inertial oscillation was a local expression of the large-scale response to the wind burst.

5. Turbulent Fluxes

Turbulent fluxes were estimated from measured values of ϵ and vertical shear using the dissipation method [e.g., *Dillon et al.*, 1989]. The method is based on the TKE equation for stationary, homogeneous turbulence, namely,

$$P + J_b = \epsilon. \tag{1}$$

The first term on the left-hand side of (1) represents the rate of TKE production by turbulent Reynolds stress, $\boldsymbol{\tau} = -\rho(\overline{u'w'}, \overline{v'w'})$, interacting with the mean vertical shear:

$$P = \frac{\boldsymbol{\tau}}{\rho} \cdot \frac{\partial \mathbf{U}}{\partial z}, \tag{2}$$

and is parameterized as $K_m Sh^2$, where K_m is the turbulent eddy viscosity. The second term on the left-hand side of (1) represents the creation (or, more usually in a stably stratified fluid, destruction) of TKE via the turbulent buoyancy flux. The flux Richardson number R_f represents the fraction of shear production that is spent increasing potential energy via negative buoyancy flux; that is, $R_f = -J_b/P$. A frequent assumption is that the value of R_f is constant (the validity of this is questioned by *Gargett and Moum* [1995] and *Moum and Gargett* [1995]). In this work, we set $R_f = 0.17$ (this is equivalent to setting the mixing efficiency, $\Gamma = J_b/\epsilon = R_f/(1 - R_f)$, to 0.2). Using (2) and the definitions of K_m and R_f, we solve (1) to obtain an expression for the turbulent viscosity in terms of the dissipation rate, namely,

$$K_m = \frac{1}{1 - R_f} \frac{\epsilon}{Sh^2}. \tag{3}$$

Near the surface, K_m exhibited the same diurnal cycle

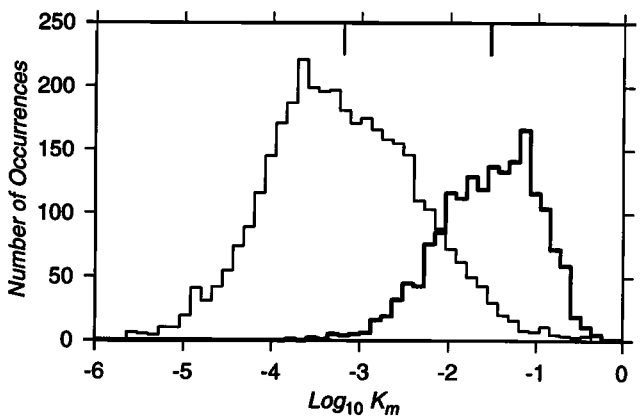

	Below DML	Within DML
Arithmetic mean	4.67×10^{-3}	5.73×10^{-2}
Geometric mean	6.36×10^{-4}	2.88×10^{-2}
Median	5.01×10^{-4}	3.16×10^{-2}
Mode	2.19×10^{-4}	7.24×10^{-2}

Figure 10. Histograms for K_m in the layer -70 m $< z < -18$ m. The thick (thin) curve corresponds to values observed within (below) the diurnal mixed layer. Vertical lines (near top) indicate the geometric mean of each subsample. Also given are various measures of central tendency for measurements made below (left) and within (right) the diurnal mixed layer (DML).

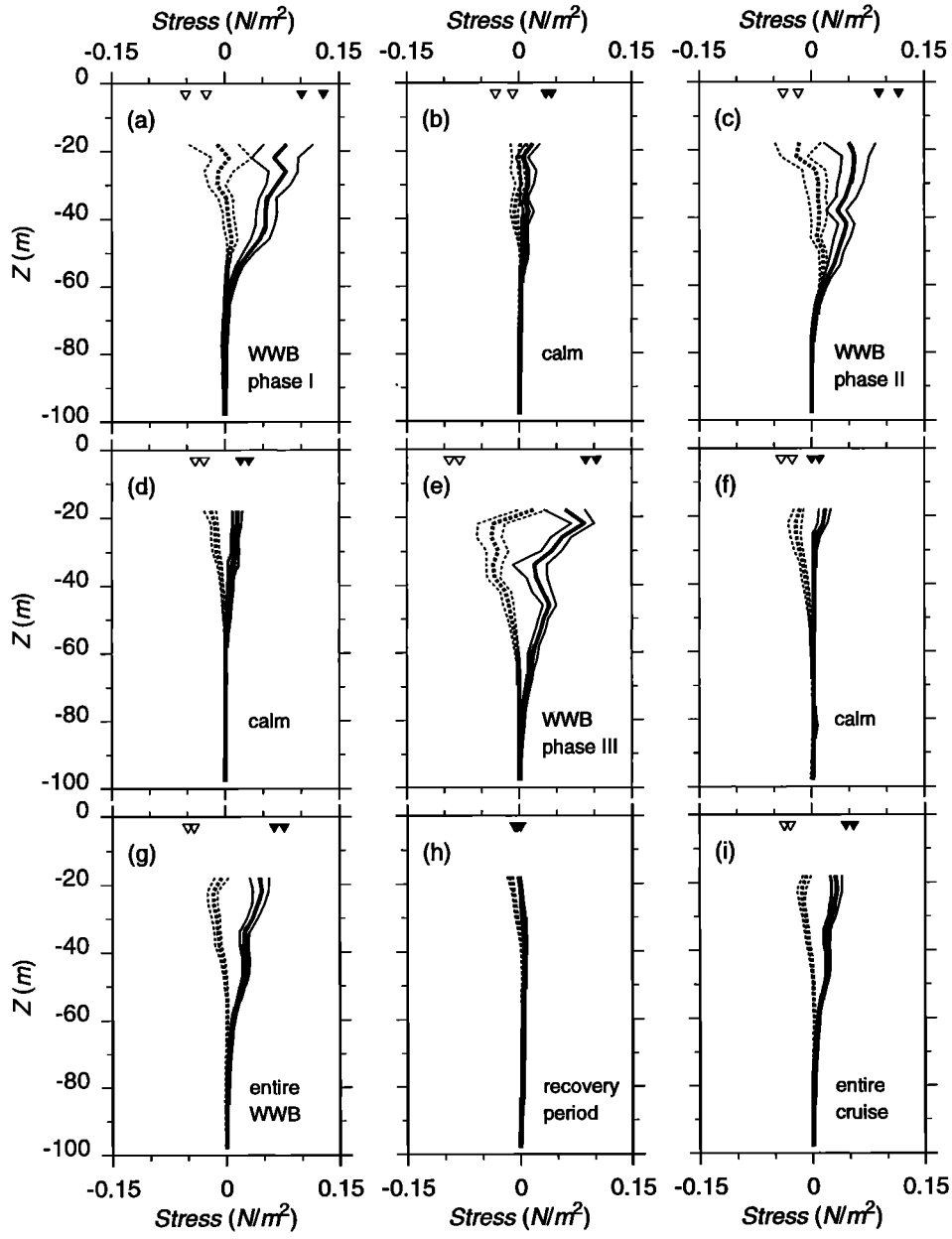

Figure 11. Time-averaged vertical profiles of the turbulent Reynolds stress. Triangles near the surface denote the surface wind stress, with the zonal (meridional) components denoted by the solid (dotted) curves and the solid (open) triangles. The spread between the triangles and that between the thin outer curves indicate 95% confidence limits on the time average: (a) t = days 355, 358; (b) t = days 358, 359.5; (c) t = days 359.5, 362; (d) t = days 362, 365; (e) t = days 365, 369; (f) t = days 369, 371; (g) t = days 355, 371; (h) t = days 371, 378; and (i) t = days 355, 378. WWB is westerly wind burst.

as did ϵ (Figure 9). The largest values of K_m were observed near the surface on windy nights. The large dissipation rates associated with the deep cycle of turbulence did not generally involve large turbulent diffusivities, because the shear in that region was intense. The regime of largest K_m coincided with the diurnal mixed layer, the depth of which is defined by a density increase of 0.01 kg m^{-3} from the surface value (SHM2). The geometric (arithmetic) mean of K_m in the upper 70 m (defined in section 4 as layer 1) was 1.2×10^{-3} (1.5×10^{-2}) m^2 s^{-1}. For comparison, *McPhaden et al.* [1988] fitted a current profile observed at the equator soon after a wind burst to a simple, constant K_m model for the equilibrium current generated by a steady westerly wind and thereby obtained the estimate $K_m \sim 10^{-2}$ m^2 s^{-1}. The assumption that K_m is constant, however, is clearly naive. The histograms of values of K_m above and below the base of the diurnal mixed layer (Figure 10) suggest separate physical regimes. Each histogram is roughly lognormal. Within the diurnal mixed layer, the geomet-

ric mean of K_m is 2.9×10^{-2} m^2 s^{-1}; below that layer, it is 6.4×10^{-4} m^2 s^{-1}. (Note that our estimates of the arithmetic mean of K_m are sensitive to the largest values observed. These values occur when the shear is close to the noise level (see Figure 5b; the error in hourly averages of Sh^2 is $\sim 10^{-6}$s^{-2}) and therefore involve large relative errors. Large values of K_m are also often found in regimes where the flow is statically unstable, so that the assumption of constant R_f in (3) is of questionable validity.)

The Reynolds stress is parameterized as $\tau = \rho K_m \partial \mathbf{U}/\partial z$. During all phases of the cruise, the Reynolds stress components were nearly zero below the top of the pycnocline (Figure 11). Above this depth, the stress components increased in a manner that suggests a good match with the surface stress, although our stress estimates become highly variable in the 18- and 22-m depth bins due to the low observed shear. The correspondence between the wind stress and shallow turbulent stresses is a test of the accuracy of the estimates of K_m discussed above. The results suggest that while hourly estimates may involve large errors, averages over a few days are probably correct to within a factor of 2. During Tropic Heat 1 (TH1), *Dillon et al.* [1989] found that the zonal component of the Reynolds stress increased exponentially toward the surface (Figure 12, circles), whereas *Hebert et al.* [1991] found depth dependence which was closer to linear during Tropic Heat 2 (TH2) (Figure 12, triangles). Both of these sets of measurements were made farther east along the equator, near 140°W; the former were in relatively constant windy conditions, and the latter were in light and variable winds. The mean wind was from the east in each case. In all three cases, the dissipation method yields estimates of the time-averaged Reynolds stress, which appear consistent with the requirement of continuity of stress at the surface. The shape of the COARE profiles resembles the TH2 results more than TH1, despite the fact that the latter experiment, like ours, was carried out in conditions of strong wind. While the depth dependence of the COARE stress profiles is similar to that observed in TH2, magnitudes are closer to TH1. Because of the extreme depth attenuation of turbulent stress found during TH1, it was hypothesized that a process other than turbulence was responsible for redistributing momentum vertically over the upper 50–100 m in order to match the depth dependence of the zonal pressure gradient and thus close the zonal momentum budget. Internal gravity waves were thought to be a prime candidate, and, indeed, these have been observed to be especially intense at this location [*Moum et al.*, 1992]. The weaker depth dependence and greater magnitude of the momentum transport due to turbulence in COARE suggests that turbulence is especially efficient at vertically transporting momentum in the upper 50 m. Continued analyses will focus on the role of internal gravity waves below 50 m during COARE.

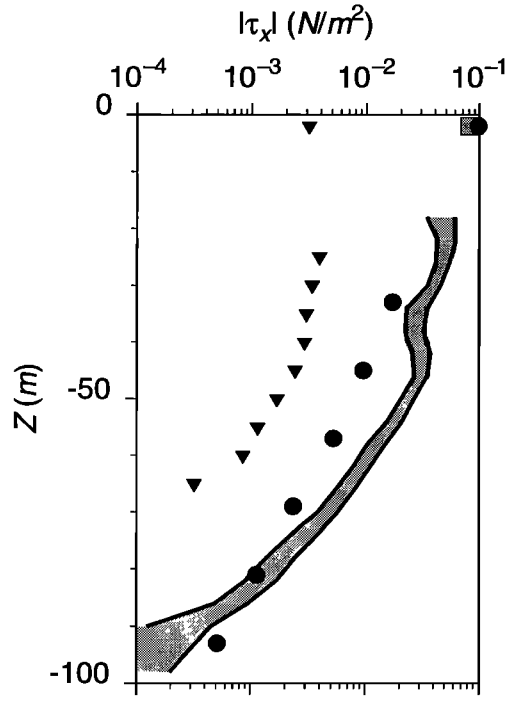

Figure 12. Zonal component of the Reynolds stress, averaged over the duration of the wind burst (shaded curve). The width of the shaded curve spans the 95% confidence limits on the time mean (from hourly values). Circles and triangles represent zonal stresses from Tropic Heat 1 and 2, respectively. (Values from the Tropic Heat experiments have been multiplied by −1 to permit log scaling.) Symbols at the surface indicate the zonal wind stress.

6. Analysis of the Momentum Balance

Further insight into the dynamic response to the wind burst may be gained via analysis of zonal and meridional momentum budgets. These budgets are constructed as follows. The usual equations for horizontal momentum conservation are integrated between two depths, z_1 and z_2, to obtain

$$\frac{\partial \overline{U}}{\partial t} = f\overline{V} + \frac{\tau_x(z_2)}{h\rho_o} - \frac{\tau_x(z_1)}{h\rho_o} + R_x; \qquad (4a)$$

$$\frac{\partial \overline{V}}{\partial t} = -f\overline{U} + \frac{\tau_y(z_2)}{h\rho_o} - \frac{\tau_y(z_1)}{h\rho_o} + R_y; \qquad (4b)$$

Here U, V is the horizontal current; f is the local Coriolis frequency; τ_x, τ_y is the Reynolds stress; and the overbar indicates a depth average over the layer whose lower and upper boundaries are z_1 and z_2, respectively. The $h = z_2 - z_1$ is the layer thickness. The background density ρ_o is given the value 1023 kg m^{-3}. For each of (4a) and (4b), the first term on the right-hand side represents the Coriolis force. The second term represents the turbulent momentum flux at the top of the layer (the wind stress if $z_2 = 0$), while the third denotes the turbulent momentum flux at the bottom of the layer. The remaining terms in the horizontal momentum equations (primarily, pressure gradient forces, vertical fluxes due to internal waves, and lateral advection) cannot be

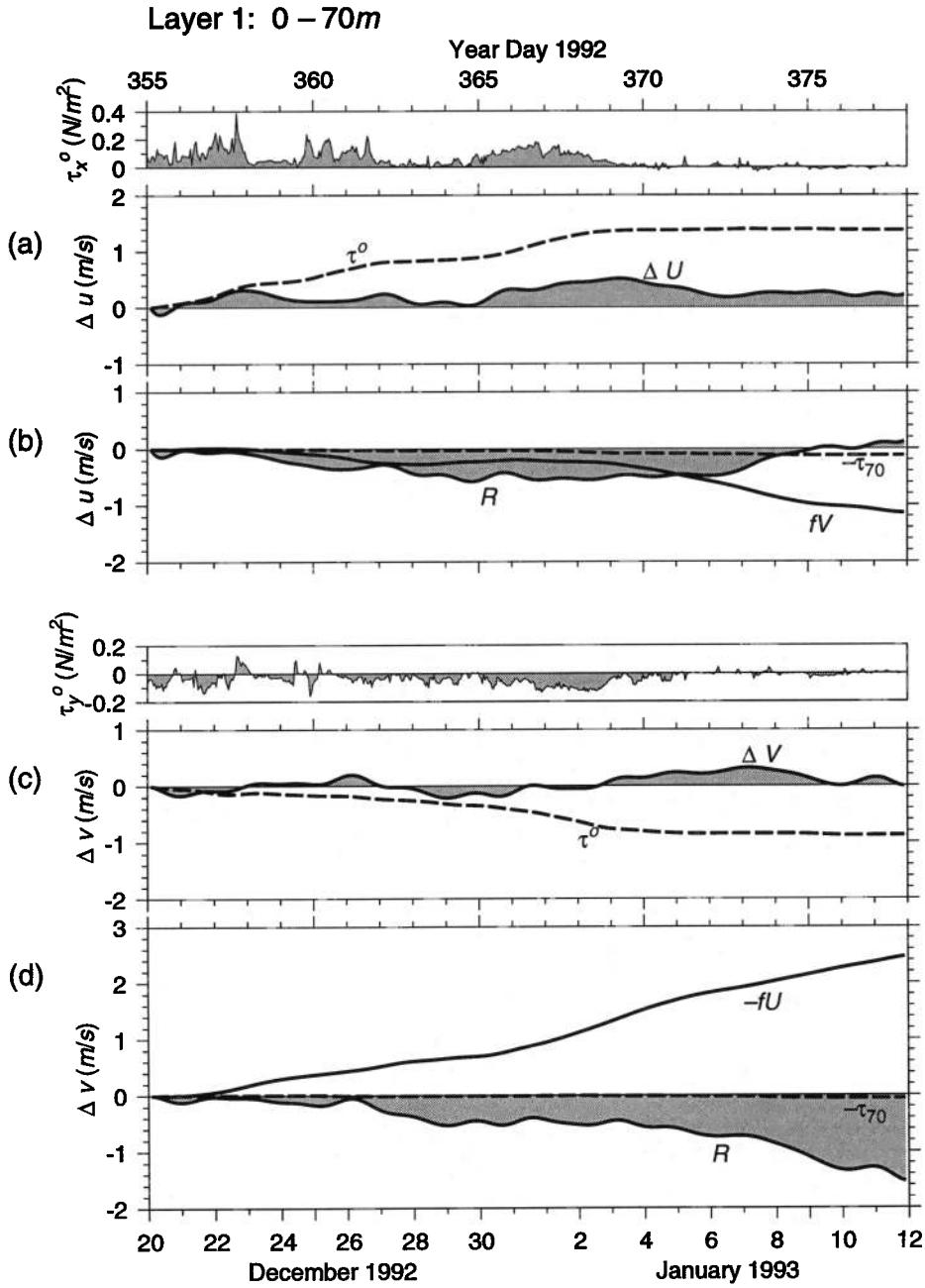

Figure 13. The momentum budget for the layer -70 m $< z < 0$ m (layer 1). (a) Cumulative (i.e., time integrated) zonal acceleration since the beginning of the station (shaded curve) and cumulative zonal momentum input from the surface (dashed curve). (b) Residual (taken to represent the zonal pressure gradient force) (shaded curve), zonal Coriolis acceleration (solid curve), and cumulative zonal acceleration due to turbulent mixing (dashed curve). (c) Same as Figure 13a, but in the meridional direction. (d) Same as Figure 13b, but in the meridional direction. Low-pass filter cutoff frequency is 1.5 cpd.

estimated reliably from our data and are instead represented as a residual force R_x, R_y, which is invoked to account for the observed acceleration. The residual also contains any errors which are present in our estimates of the other forces appearing in the budget.

The cumulative momentum budget is obtained by integrating in time from the beginning of the observation period to obtain net changes in vertically averaged velocity, namely,

$$\Delta(\overline{U}, \overline{V}) = \int_0^t \frac{\partial}{\partial t}(\overline{U}, \overline{V})dt, \tag{5}$$

where overbars indicate the vertical average between z_1 and z_2 which appears in (4a) and (4b). The cumulative budget is employed in order to allow easy visual assessment of the time-integrated contribution of each term.

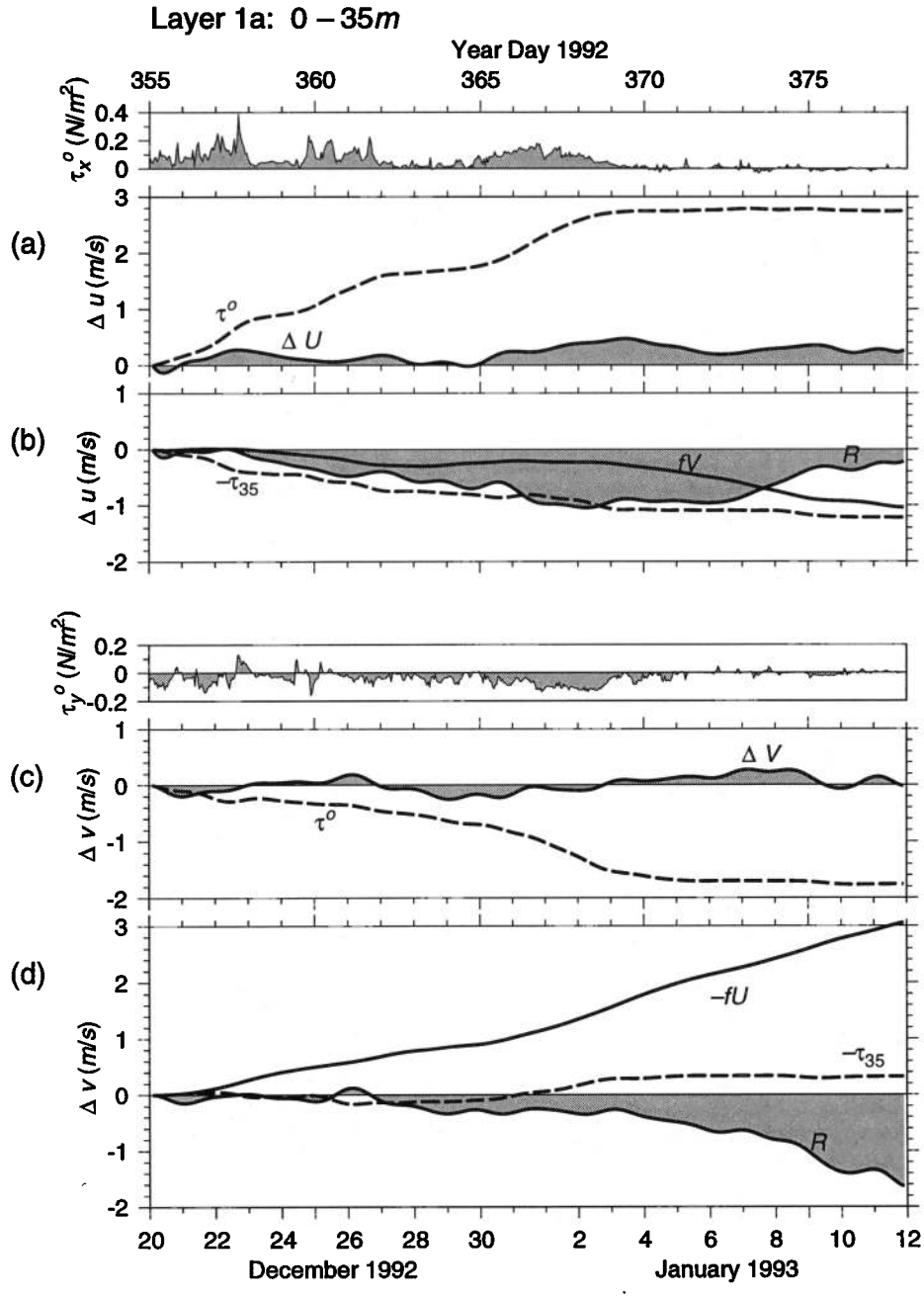

Figure 14. Same as Figure 13, but for -35 m $< z < 0$ m.

Fluctuations due to the diurnal mixing cycle and the semidiurnal tide were removed by means of a low-pass filter with cutoff frequency equal to 0.75 cpd.

We evaluate the terms in the momentum equations for several layers, beginning with the 70-m-thick surface layer dominated by wind-driven currents and identified in section 4 as layer 1 (Figure 13). During the first phase of the wind burst (t = days 355–358), zonal momentum transferred from the wind accounts almost identically for the observed acceleration of the currents in this layer. At the end of phase 1, an immediate deceleration of the eastward flow was driven primarily by the residual force. Following *McPhaden et al.* [1988], we hypothesize that the residual is mainly a measure of the pressure gradient force, in which case the appearance of the residual at the end of phase 1 suggests that the eastward flow generated an adverse pressure gradient in the near-surface region. *Zhang* [1995] has simulated the response to WWB-like forcing and has noted the development of an adverse pressure gradient whose magnitude is similar to that of our residual. During phase 2, the action of the Coriolis force greatly reduced the effect of the eastward wind stress. During phases 1 and 2 and in the intervening period of calm winds, the meridional current exhibited a steady northward acceleration which was driven by the Coriolis force and opposed by both the surface wind stress and the residual. It is the Coriolis turning of this northward current which

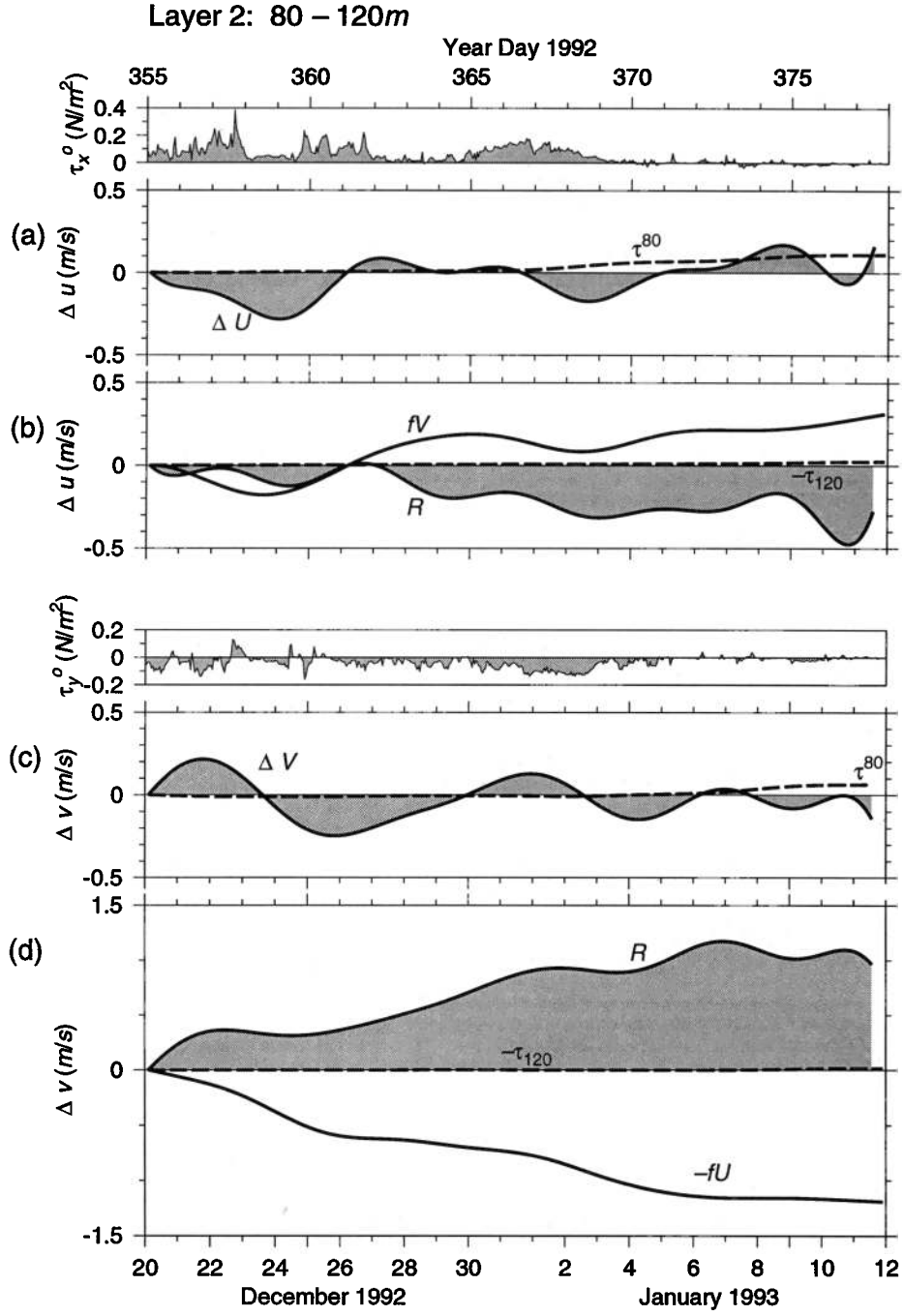

Figure 15. Same as Figure 13, but for layer 2 (-120 m $< z < -80$ m) and cutoff frequency of 0.25 cpd.

accounts for the attenuated response of the zonal current to wind forcing during phase 2. It appears, then, that the eastward acceleration which arose due to the zonal wind during phase 1 generated a response in the Coriolis and pressure gradient terms which opposed the wind-driven zonal acceleration during phase 2. In other words, phase 2 arrived out of phase with the wave wake generated by phase 1, and the resulting eastward acceleration was reduced correspondingly.

Because of the destructive interference between the wind stress during phase 2 and the wave wake from phase 1, the near-surface region was close to a state of motionless equilibrium when phase 3 began (although Coriolis turning of the southward meridional current accelerated the zonal flow slightly during days 363–365). The response to the wind stress during phase 3 was therefore not greatly complicated by interference effects, and the observed eastward acceleration of the near-surface currents ($\sim$0.2 m s^{-1} from day 365 to day 368) closely parallels the momentum input from the wind. We can now advance an explanation for the out-of-proportion response of the surface currents to the

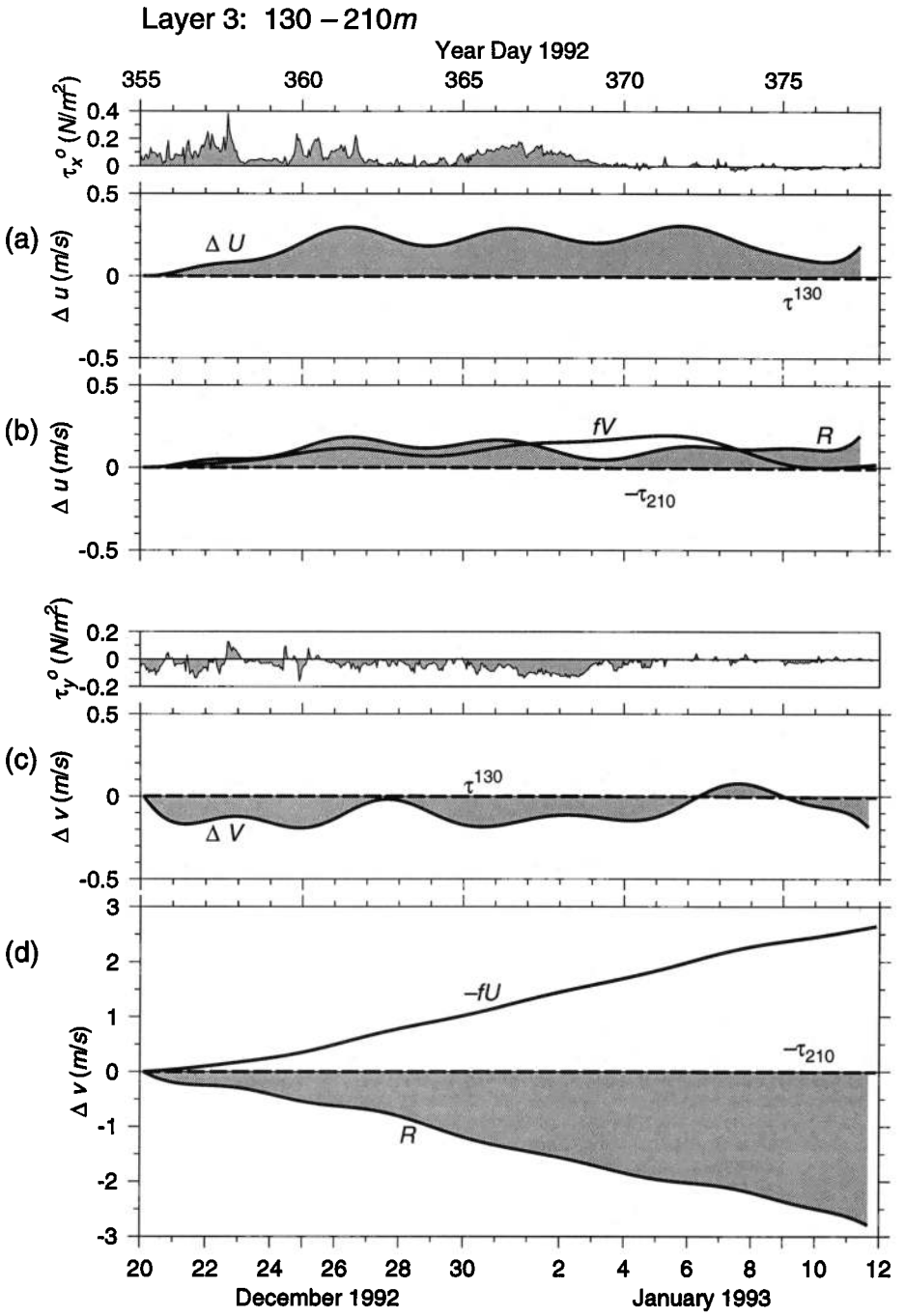

Figure 16. Same as Figure 13, but for layer 3 (-210 m $< z < -130$ m) and cutoff frequency of 0.25 cpd.

separate phases of the WWB; the response to phase 1 was truncated by an adverse zonal pressure gradient, while the response to phase 2 was attenuated by the Coriolis force. The eastward acceleration in response to phase 3 was almost perfectly consistent with the amount of wind forcing. This eastward acceleration led to a strong northward Coriolis force, which accelerated the meridional current in opposition to the northerly wind. As the strong eastward wind subsided (days 369–371), the Coriolis force associated with the meridional current acted to decelerate the near-surface zonal flow. During the succeeding few days, however, a zonal residual force arose which opposed the Coriolis force and maintained the eastward jet in a state of approximate equilibrium during the remainder of the station. The eastward residual force which is evident during days 372–375 coincided with the appearance of the long-lived jet following the wind burst. During days 374 and 375, both the zonal residual and the Coriolis force decreased as the northward meridional current decelerated. The near balance between Coriolis and residual forces is apparent in the meridional direction, as well as in the zonal.

As we expect based on the Reynolds stress profiles

(Figure 11), the turbulent momentum flux at $z = -70$ m played a negligible role in governing the mean currents in layer 1 (Figure 13). However, it played a crucial role in distributing the momentum input at the surface, as well as that generated at particular depths by other forces, throughout the layer. This is illustrated in Figure 14, which shows the cumulative momentum budget for the layer between the surface and $z = -35$ m. Here the distribution of wind stress, Coriolis, and residual forces is qualitatively similar to that seen in the 70-m layer, but the turbulent momentum flux across the surface $z = -35$ m now plays a central role. During phase 1 of the wind burst, only about one half of the eastward momentum input at the surface appeared in the current above 35 m; the remainder was transferred to the deeper region by the turbulent stress. Throughout the remainder of the wind burst (days 358–370), the zonal turbulent stress acted continuously to transfer eastward momentum to the region below $z = -35$ m. In the meridional direction, the northward Coriolis-driven acceleration was amplified by the action of the turbulent stress. This was because the region below $z = -35$ m was unaffected by the southward surface stress and therefore responded more rapidly to the northward Coriolis acceleration than did the region nearer the surface. Subsequently, northward momentum was transferred from the lower to the upper layer via the turbulent stress.

We turn next to the momentum budget for the layer between 80 and 120 m depth. Our purpose is to describe the dynamics of the westward jet that is apparent in this layer (see Figure 4). A weak westward jet ($\sim$0.1 m s^{-1}) was in place at the beginning of our cruise and had apparently been present since leg 1 [*Wijesekera and Gregg,* 1996]. During our cruise, the velocity of the jet varied by $\sim$0.3 m s^{-1} on a timescale of $\sim$10 days. Since these accelerations are clearly associated with the near-inertial oscillation discussed above, we have low-pass filtered the terms in the cumulative momentum budget with a cutoff frequency of 0.25 cpd in order to more clearly display the low-frequency dynamics. The initial accelerations in this layer are to the west and the north (Figure 15). These accelerations are driven by the Coriolis force and the meridional residual force, respectively. The meridional balance during the remainder of the wind burst suggests that the westward jet is held in approximate geostrophic equilibrium between the southward Coriolis force and a northward pressure gradient force. Both the Coriolis and the residual terms oscillate about this equilibrium with a period of 10–12 days, but the oscillation in the residual leads that in the Coriolis force by 90°. The resulting imbalance between the Coriolis force and the residual drives the wavelike meridional accelerations visible in Figure 4. The zonal accelerations associated with the "reversing jets" seen in Figure 4 are also driven by a wavelike alternation of Coriolis and residual forces.

The momentum budget for the layer between $z = 130$ m and $z = 210$ m is shown in Figure 16. Again, we have low-pass filtered the results with cutoff frequency 0.25 cpd in order to more clearly display the dynamics at subdiurnal frequencies. The meridional momentum budget suggests that undercurrent was held in a state of approximate geostrophic equilibrium between the southward pressure gradient force and the northward Coriolis force. The zonal budget shows that the undercurrent was accelerated during the first half of the wind burst, then decelerated over several days following the end of the wind burst, by a combination of Coriolis and residual forces. Again, turbulent momentum fluxes are negligible at these depths.

7. Discussion

A three-phase westerly wind burst occurred in the Western Pacific Warm Pool between December 20, 1992, and January 4, 1993. Nearly 500 mm of rain fell during this period, and SST dropped by 1°C. The upper 50 m of the water column was well mixed from the outset, remained so during the wind burst, but quickly restratified when the heavy weather subsided.

Our purpose here has been to learn what we can about the ocean's response to the wind burst from the one-dimensional data gathered aboard the *Moana Wave.* A fuller understanding must await analysis of basin-scale data and model output. Our interpretations of one-dimensional data in terms of horizontal pressure gradients, for example, are speculative at this point. Nevertheless, we have found it possible to construct a hypothetical scenario which is consistent with both the one-dimensional data and our current theoretical understanding of equatorial dynamics, and we present this scenario as a guide for future analyses.

The dynamic response to the wind burst was dominated by wavelike motions in the near-inertial band. In addition, an eastward surface jet with average speed 40 cm s^{-1} persisted for at least 1 week following the cessation of strong winds. Despite the low latitude of the COARE region ($\phi \sim 2°$S), the Coriolis force played a crucial role in the dynamics. Analysis of the momentum budget for the upper 70 m has shown how the response of the surface currents to wind forcing is controlled by interference between the instantaneous wind stress and the oscillatory wake left by previous wind stress. This interference effect greatly attenuated the response to phases 1 and 2, but it amplified and prolonged the response to phase 3.

Mixing played a crucial role in distributing momentum above the thermocline, as has been shown via the momentum budget for the upper 35 m. If the balance we hypothesize (Coriolis versus pressure gradient) below that depth holds, then it also is not necessary for internal waves to transport significant momentum, as has been found farther east along the equator. The magnitude of K_m in the diurnal mixed layer is approximately (within a factor of 3) that obtained by *McPhaden et al.* [1988] in their constant-K model of WWB-generated flow. Below this layer, however, K_m is more than a factor of 10 smaller.

The westward jet centered at 100 m (layer 2) appeared initially during leg 1, coinciding with a weak wind event which was observed on days 330–333 [*Wijesekera and Gregg,* 1996]. During the December wind burst, this current exhibited strong oscillations. The initial acceleration was to the north and appeared as part of the residual in our one-dimensional momentum budget. This acceleration might be attributable to a southward pressure gradient, though it is unclear how such a gradient could have originated. Coriolis turning of the resulting northward current drove the initial intensification of the westward jet on days 357 and 358. Further accelerations appear as out-of-phase oscillations in the residual (pressure gradient) force and the Coriolis force. In the layer containing the EUC (layer 3; see Figure 16), the strongest accelerations by far were the meridional Coriolis and residual forces which maintained the EUC in approximate (presumably geostrophic) equilibrium. However, oscillations in the subinertial band were present in this depth range as well.

Acknowledgments. We are grateful to Chris Fairall and George Young for sharing meteorological data and computed fluxes with us; to Mike Gregg for allowing us to use his CTD for daily comparisons with CHAMELEON temperature and conductivity profiles; to Doug Caldwell and to the anonymous reviewers for comments on early versions of the manuscript; to Mike Neeley-Brown, Ray Kreth, Ed and Colleen Llewellyn, Sue Young, Chaojiao Sun, Bill Freer, and Walt Waldorf for engineering and at-sea support for this project; and to our families for allowing us to be at sea during Christmas. This work was supported by the National Science Foundation (OCE 9110552).

References

Delcroix, T., G. Eldin, M.J. McPhaden, and A. Morliere, The effect of westerly windbursts upon the western equatorial Pacific ocean, February-April 1991, *J. Geophys. Res., 98,* 16,379–16,385, 1993.

Dillon, T.M., J.N. Moum, T.K. Chereskin, and D.R. Caldwell, Zonal momentum balance at the equator, *J. Phys. Oceanogr., 19,* 561–570, 1989.

Efron, B., and R.J. Tibshirani, *An Introduction to the Bootstrap,* Chapman and Hall, New York, 1993.

Eriksen, C.C., Equatorial ocean response to rapidly translating windbursts, *J. Phys. Oceanogr., 23,* 1208–1230, 1993.

Fairall, C., E.F. Bradley, D.P. Rogers, J.B. Edson, and G.S. Young, The TOGA COARE bulk flux algorithm, *J. Geophys. Res., 101,* 3747–3764, 1996.

Gargett, A.E., and J.N. Moum, Mixing efficiencies in turbulent tidal fronts: Results from direct and indirect measurements of density flux, *J. Phys. Oceanogr., 25,* 2583–2608, 1995.

Hebert, D., J.N. Moum, C.A. Paulson, D.R. Caldwell, T.K. Chereskin, and M.J. McPhaden, The role of the turbulent stress divergence in the equatorial Pacific zonal momentum balance, *J. Geophys. Res., 96,* 7127–7136, 1991.

Lien, R.-C., M.J. McPhaden, and D. Hebert, Intercomparison of ADCP measurements at 0°, 140°W, *J. Atmos. Oceanic Technol., 11,* 1334–1349, 1994.

Lukas, R., and E. Lindstrom, The mixed layer of the western equatorial Pacific ocean, *J. Geophys. Res., 96,* 3343–3357, 1991.

McPhaden, M.J., and J. Picaut, El Niño-Southern Oscillation displacements of the western equatorial Pacific warm pool, *Science, 250,* 1385–1388, 1990.

McPhaden, M.J., H.P. Frietag, S.P. Hayes, B.A. Taft, Z. Chen, and K. Wyrtki, The response of the equatorial Pacific Ocean to a westerly wind burst in May 1986, *J. Geophys. Res., 93,* 10,589–10,603, 1988.

McPhaden, M.J., F. Bahr, Y. du Penhoat, E. Firing, S.P. Hayes, P.P. Niiler, P. L. Richardson, and J.M. Toole, The response of the western equatorial Pacific Ocean to westerly wind bursts during November 1989 to January 1990, *J. Geophys. Res., 97,* 14,289–14,303, 1992.

Moum, J.N., and D.R. Caldwell, Experiment explores the dynamics of ocean mixing, *Eos Trans. AGU, 75,* 489–490, 495, 1994.

Moum, J.N., and A.E. Gargett, Mixing efficiencies in stratified fluids: Data from the main thermocline and a turbulent tidal front, paper presented at 11th Symposium on Turbulence and Diffusion, Am. Meteorol. Soc., Boston, Mass., 1995.

Moum, J.N., D.R. Caldwell, and C.A. Paulson, Mixing in the equatorial surface layer and thermocline, *J. Geophys. Res., 94,* 2005–2021, 1989.

Moum, J.N., M.J. McPhaden, D. Hebert, H. Peters, C.A. Paulson, and D.R. Caldwell, Internal waves, dynamic instabilities and turbulence in the equatorial thermocline: An introduction to three papers in this issue, *J. Phys. Oceanogr., 22,* 1357–1359, 1992.

Moum, J.N., M.C. Gregg, R.-C. Lien, and M.-E. Carr, Comparison of turbulent kinetic energy dissipation rates from two ocean microstructure profilers, *J. Atmos. Oceanic Technol., 12,* 346–366, 1995.

Schudlich, R.R., and J.F. Price, Diurnal cycles of current, temperature and turbulent dissipation in a model of the equatorial upper ocean, *J. Geophys. Res., 97,* 5409–5422, 1992.

Smyth, W.D., D. Hebert, and J.N. Moum, Local ocean response to a multiphase westerly wind burst, 2, Thermal and freshwater responses, *J. Geophys. Res.,* this issue.

Webster, P.J., and R. Lukas, TOGA COARE: The coupled ocean-atmosphere response experiment, *Bull. Am. Meteorol. Soc., 73,* 1377–1415, 1992.

Weller, R.A., and S.P. Andersen, Temporal variability and mean values of the surface meteorology and air-sea fluxes in the western equatorial Pacific warm pool during the TOGA Coupled Ocean-Atmosphere Response Experiment, *J. Clim.,* in press, 1996.

Wijesekera, H.W., and M.C. Gregg, Mixing in the western equatorial Pacific during the first leg of TOGA-COARE, *J. Geophys. Res., 101,* 977–998, 1996.

Zhang, Q., The oceanic response to atmospheric forcing in the western equatorial Pacific, Ph.D. dissertation, Univ. of R. I., Narragansett, 1995.

D. Hebert, Graduate School of Oceanography, University of Rhode Island, Narragansett, RI 02882.

J. N. Moum and W. D. Smyth, College of Oceanic and Atmospheric Sciences, Oregon State University, 104 Ocean Administration Building, Corvallis, OR 97331. (e-mail: smyth@oce.orst.edu)

(Received May 30, 1995; revised May 10, 1996; accepted May 15, 1996.)